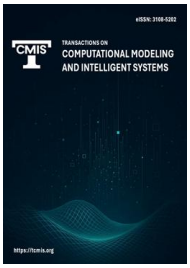

Transactions on
Computational Modeling and Intelligent Systems

Volume 3, April 2026, Article 10059
https://doi.org/10.65112/tcmis.10059

eISSN: 3108-5202
www.tcmis.org

RESEARCH ARTICLE

Thermal and flow characteristics of MHD Williamson hybrid nanofluid under activation energy in a porous asymmetrical peristaltic channel

Hanumantha Hanumantha[1], Shivaraya Keriyappa[2], Mallanagoud Mulimani[3*], Ali J Chamkha[4], Kumbinarasaiah Srinivasa[5], Suneetha Kolasani[6], and Rathod Kirankumar Gulab[7]

[1] *Department of Mathematics, Adikavi Sri Maharshi Valmiki University, Raichur, 584133, Karnataka, India.*
[2] *Department of Mathematics, Government First Grade College Soraba, 577429, Karnataka, India.*
[3] *Department of Applied Sciences, Faculty of Engineering and Technology, Khaja Bandanawaz University, Kalaburagi, 585104, India.*
[4] *Faculty of Engineering, Kuwait College of Science and Technology, 35004, Doha District, Kuwait.*
[5] *Department of Mathematics, Bangalore University, 560056, Bengaluru, India.*
[6] *Department of Mathematics, Ballari Institute of Technology and Management, Ballari, 583104, Karnataka, India.*
[7] *Department of Mathematics, PG Centre Aland, Gulbarga University, Aland, 585302, Karnataka, India.*

[*] *Corresponding Author. Email: mallanagoudmulimani@gmail.com, mulimani@kbn.university (M. Mulimani)*

Article Information

Received: 15 January 2026
Accepted: 8 April 2026
Published: 13 April 2026

AMS 2020 Classification: 35C05, 76A05, 76S05, 76W05, 80A20

Abstract

The importance of the behavior of thermodynamics and the movement of fluids in the present day, especially to improve the effectiveness of operations in the domains of medical and engineering sciences, e.g., cooling of microchips, lubrication, cancer treatment, drug delivery, and so on, cannot be emphasized enough. Hybrid nanofluids have been a subject of significant academic interest, considering their improved thermal conductivity and other properties related to the transport of energy, differentiating them from other fluid media. However, the complex nature of the hybrid nanofluids' behavior, considering the impact of the modified Darcy principle, Lorentz force, Hall effects, activation energy, and Joule heating, has yet to be explored, especially for non-Newtonian fluids, i.e., Williamson fluids. The main goal is to investigate the peristaltic motion of a magnetohydrodynamic (MHD) Williamson hybrid nanofluid in a horizontal, permeable, asymmetric channel under a magnetic field. The Buongiorno nanofluid model is used to study the effects of thermophoresis and Brownian motion. The energy and concentration equations are derived by considering the effects of Joule heating, viscous dissipation, and activation energy. No-slip boundary conditions are applied at the channel boundaries. The lubrication approximation method is used, and the problem is solved using the homotopy perturbation method (HPM). Physical quantities are examined with the help of graphs and tables. The velocity increases with the Darcy parameter and Hall current parameter on both channel walls. However, the velocity decreases with the magnetic parameter. An increase in the values of the Brownian motion parameter and the thermophoresis parameter results in an increase in the temperature of the fluid. Similarly, an increase in the values of the activation energy parameter results in an increase in the concentration. In addition, the thermal properties of the hybrid nanofluid are superior to those of the standard nanofluid. The results obtained are applicable to thermal engineering, nuclear engineering, roller pumps, heat transfer devices, and chemical engineering.

Keywords: Activation energy, modified Darcy's law, nanofluid, MHD, peristaltic flow, Brownian and thermophoretic movement.

1. Introduction

Nanofluids have attracted a lot of interest in the field of biomedical engineering in recent years. Nanofluids, which are suspensions of nanoparticles in base fluids, have been widely used to improve thermal properties. In their study, Choi and Eastman coined the term "nanofluid" [1]. Researchers have started experimenting with mixing

different materials' nanoparticles into a base fluid to enhance its thermal properties. Typical nanoparticle constituents include metals, carbides, and oxides, all of which have high thermal conductivities. In the meantime, ethanol, water, oil, and ethylene glycol are typical examples of base fluids. Nanofluids are now being used in a wide range of advanced biomedical research and therapy. In the nanofluid size spectrum, the ratio of particle surface area to particle volume is so high that interactions are controlled by short-range forces, such as surface forces and van der Waals attraction. Buongiorno [2] conducted a comprehensive analysis of convective transport phenomena in nanofluids and identified Brownian motion and thermophoresis as the principal mechanisms responsible for the marked enhancement in heat transfer. Subsequently, Tiwari and Das [3] investigated nanofluidic transport by incorporating the size of tiny materials, thermal conductivity, viscosity, and volume fraction into the nanofluid heat transfer mechanism. Although nanofluids exhibit significant potential, they are also associated with particular limitations regarding stability and thermal conductivity, which has led scholars to explore the properties of hybrid nanofluids. Hybrid nanofluids are composed of different types of nanoparticles and thus have improved thermophysical characteristics. Reddy and Makinde [4] explore the impact of MHD on the peristaltic mechanism of Jeffrey nanofluid over an asymmetric channel. Recently, Vaidya et al. [5, 6] investigated the behaviour of hybrid nanoparticle suspension in viscous blood flow in constricted arteries and concluded that the enhanced thermal properties of nanoparticles help to control the blood flow during the surgery. Divya et al. [7] proposed the study of Williamson hybrid nanofluid flow under the influence of a magnetic field and thermal radiation. Some recent investigations in this direction may also be observed through references [8, 9].

The physiological features of permeable media and their main implications in areas like metallurgy and geosciences have driven enhanced interest in the peristaltic mechanism. Samples of permeable media in biological systems contain arterial blockages, obstacles in brain cells, bile ducts, the bladder, and blood vessels. Although Darcy's law is extensively used to tackle the impact of permeable media, its core application to flows of both viscous and non-Newtonian fluids is not realistic, as non-Newtonian fluids display physiological natures different from those of purely viscous materials. Subsequently, a modified skeleton of Darcy's law that combines these rheological influences is critical for precisely portraying non-Newtonian flows in a permeable medium. Prior studies have engineered this rectification in the situation of non-Newtonian peristalsis via porous media [10, 11]. In biological and physiological contexts, understanding peristaltic motion under MHD effects is significant. In conductive fluids, a strong magnetic field produces electrical currents, which alter flow patterns. More equipment, such as blood pumps, heat exchangers, flow meters, and control generators, as well as medical applications including intraoperative blood flow regulation, magnetic tracer enhancement, and hyperthermia therapy, relies on MHD principles. Many magnetotherapy scenarios include non-Newtonian MHD flows. MHD-driven peristaltic studies frequently focus on processes such as urine transport through the ureter, blood circulation in arteries, and tissue or cellular changes. In the case of a strong magnetic field, the inspection of Hall's influence becomes very significant. These effects have maximum application in many fields that encompass devices like power generators, magnetometers to measure the magnetic field, transformers, Hall current sensors, automotive fuel level indicators, magnetic situation sensing in DC electric motors, and spacecraft propulsion. Motivated by these applications, numerous researchers have examined MHD-influenced peristaltic transport across different geometries [12, 13].

Peristalsis is attributed to the rhythmic sequence of contractions and relaxations in the walls of a distensible channel, producing wave-like movements that drive the muscle-controlled transport of fluid. In biological systems, this mechanism plays a vital role in various physiological functions, such as propelling food through the oesophagus, moving chyme along the intestines, circulating intrauterine fluid, transporting bile, facilitating sperm motion in the male reproductive tract, and moving ova through the fallopian tubes. This natural pumping process has inspired the design of roller pumps, which allow fluid transport without direct contact with mechanical components, thereby minimizing contamination risks. The pioneering study on the peristaltic mechanism was carried out by Latham [14], laying the groundwork for its integration into contemporary medical technologies, including heart–lung machines, dialysis units, and both finger and roller pumps. Jaffrin and Shapiro [15] presented a foundational theoretical and experimental framework for peristaltic flow, while Rath [16] explored different forms of peristaltic waves and their distinct characteristics through experimental analysis. Furthermore, Srivastava and Srivastava [17] investigated the detailed dynamics of peristaltic motion using both experimental and theoretical approaches. More recent advancements in peristalsis research can be found in the works cited in [18, 19].

Pseudoplastic (shear-thinning) substances are a category of non-Newtonian fluids whose viscosity decreases with increasing shear rate, causing them to behave in a plastic-like manner. Common examples include ketchup, yogurt, whipped cream, molasses, nail polish, latex paint, and blood. Unlike ideal plastic fluids, pseudoplastic fluids exhibit no yield stress. A well-known mathematical representation of such behavior is the Williamson model, first proposed by Williamson [20]. In this model, the apparent viscosity begins at μ_0 under zero-shear conditions and progressively decreases to μ_∞ as the shear rate approaches infinity. The Williamson fluid model is often applied to analyze the influence of the Weissenberg number, which represents the ratio of elastic to viscous forces. Among the earliest studies on Williamson fluid peristaltic flow were those by Nadeem and Akram [21]. Eldabe et al. [22] elucidated the MHD peristaltic transport phenomena of a Williamson nanofluid within an asymmetrical channel, considering a non-permeable region, while integrating effects such as Hall phenomena, viscous dissipation, and Ohmic heating. Rashid et al. [23] utilized the HPM to resolve the momentum equation that governs the MHD peristaltic motion of Williamson fluid within a curved tubular configuration. A plethora of additional studies have also investigated the dynamics of various non-Newtonian fluid models [24-26].

The Swedish scientist Svante Arrhenius coined the phrase “activation energy” in 1889. It speaks of the bare minimum of energy needed for molecules or atoms to start a chemical reaction. Activation energy is important in chemical engineering, geothermal reservoirs, suspension emulsions, and water treatment procedures, especially in the heat and mass transfer related to binary chemical reactions. Bestman conducted the first research on activation energy in binary chemical processes [27]. Later, Hayat et al. [28] examined entropy generation and activation energy effects in the mixed convective peristaltic transport of Sutterby nanofluids. Maimona et al. [29] investigated activation energy in peristaltic flow through porous-walled channels, while Abdelmoneim et al. [30] explored Williamson nanoliquid flow incorporating activation energy under modified Darcy’s law. Furthermore, Waqas et al. [31] portray the combined effects of activation energy and bioconvection in second-grade nanoliquids.

The existing literature witnessed that the complex behavior of the hybrid nanofluid, considering the effect of the modified Darcy principle, Lorentz force, Hall effects, activation energy, and Joule heating, still needs to be explored, particularly for non-Newtonian fluids, i.e., Williamson fluids. To bridge this existing research gap, the present investigation on the flow nature of a pseudoplastic hybrid nanofluid’s behavior has been categorized based on the Williamson fluid model. The fluid flow has been modeled by considering the fluid trapped within a horizontal channel with a peristaltic motion on the walls. The analysis considers the effect of an external magnetic field and Joule heating. Additionally, the channel has been embedded with a porous medium considering the advanced Darcy’s law, where the apparent viscosity of the shear thinning/thickening fluid has been considered instead of Newtonian fluid viscosity. To analyze the real-time fluid flow, the interaction between the nanoparticles has been considered. Additionally, the effect of chemical reactions with activation energy has been considered to analyze the chemical reactions under complex physical conditions. Overall, the study confirms that the collective improvement of thermal performance in peristaltic transport systems is achieved through hybrid nanoparticle dispersion, porous permeability, and non-Newtonian elasticity. These results highlight the potential of Williamson hybrid nanofluids for biomedical pumping mechanisms, microfluidic transport devices, and thermal management systems operating under MHD conditions.

2. Problem definition

This study examines the two-dimensional, electrically conducting peristaltic transport of a viscous, incompressible hybrid nanofluid through an asymmetric horizontal permeable channel, influenced under an externally applied magnetic field. The system is demonstrated by a Cartesian coordinate framework $(\bar{X}, \bar{Y})$, where $\bar{X}$-axis aligns with the direction of flow and the $\bar{Y}$- axis is oriented normal to it. A schematic view of the physical configuration is shown in Fig. 1. A uniform magnetic field of intensity B_0 acts normally in the direction of flow. The lower wall $\overline{H_2}$ is regulated at a fixed temperature T_1 and solute concentration C_1, while the upper wall $\overline{H_1}$ is kept at a temperature T_0 and C_0, facilitating the analysis of heat and mass transfer processes. The mathematical descriptions of the upper and lower channel boundaries are defined as follows:

$$\overline{H_1}(\bar{X}, \bar{t}) = p_1 + q_1 Cos\left[\frac{2\pi}{\lambda}(\bar{X} - c\bar{t})\right] \tag{1}$$

$$\overline{H_2}(\bar{X}, \bar{t}) = -p_2 - q_2 Cos\left[\frac{2\pi}{\lambda}(\bar{X} - c\bar{t}) + \phi\right] \tag{2}$$

In this context, $p_i(i = 1,2)$ and $q_i(i = 1,2)$ are denotes the upper and lower channel widths and wave amplitudes, respectively. the variable $\bar{t}$ denotes the time, and ϕ is the phase difference taking the values between 0 to π. If $\phi = 0$ indicates that the waves are completely out of phase, whereas if $\phi = \pi$ corresponds to the waves being in phase. moreover, p_i, q_i and ϕ satisfied the condition $q_1^2 + q_2^2 + 2q_1q_2Cos\phi \leq (p_1 + p_2)^2$.

When an external magnetic field strength B_0 interacts with the moving charged nanofluid particles within a channel, generating an electromotive force known as the Lorentz force. The generalized Ohm's law expression of fluid flow with Hall current phenomena can be written as

$$\vec{J} = \sigma_{hnf}(\vec{E} + \vec{q} \times \vec{B}) - \frac{m}{B_0}(\vec{J} \times \vec{B}) \tag{3}$$

Here, the variables are defined as follows: $\vec{q} = (\overline{U}, \overline{V}, 0)$ denotes the velocity vector, σ_{hnf} represents the effective electrical conductivity of the hybrid nanofluid, $\vec{J}$ stands for the current density $\vec{B} = (0,0,B_0)$ is the magnetic field vector, m is the Hall parameter, and $\vec{E}$ corresponds to the electric field vector.

The Maxwell's MHD constraints are as follows:

$$\nabla \times \vec{E} = -\frac{\partial \vec{B}}{\partial t}, \nabla.\vec{B} = 0, \ \nabla.\vec{J} = 0. \tag{4}$$

By neglecting the applied and induced electric fields, the Lorentz force formulation can be made simpler, as follows:

$$\vec{J} \times \vec{B} = \left(-\frac{\sigma_{hnf}B_0}{(1+m^2)}\overline{U}, -\frac{\sigma_{hnf}B_0}{(1+m^2)}\overline{V}\right). \tag{5}$$

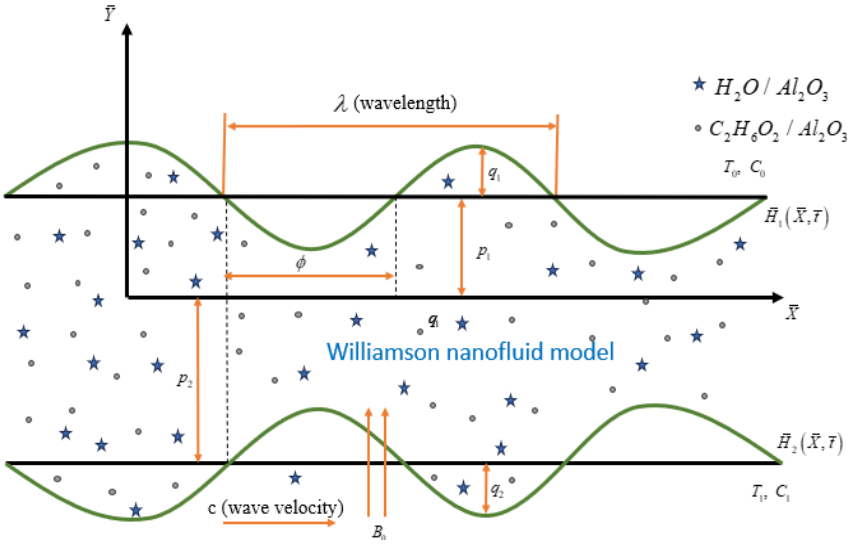

Figure 1. Configuration of fluid flow problem.

Based on the above assumptions, the equations are derived from various conservation laws, such as conservation of mass, momentum, energy, and nanoparticle concentration. The equation for conservation of mass is given by the continuity Eq. (6), where the conservation of an incompressible nanofluid is satisfied. The momentum Eqs. (7-8), developed according to the Williamson fluid formulation, is used to describe the characteristics of a shear-thinning fluid. The equation for conservation of energy (9) is employed to characterize the heat transfer behavior of the system. The equation for conservation of nanoparticle concentration (10) is developed according to the Buongiorno model, where Brownian motion and thermophoresis effects are taken into consideration. These basic equations that describe the flow behavior are presented below [21]:

$$\frac{\partial \overline{U}}{\partial \overline{X}} + \frac{\partial \overline{V}}{\partial \overline{Y}} = 0 \tag{6}$$

$$\rho_{hnf}\left(\frac{\partial}{\partial \bar{t}}+\bar{U}\frac{\partial}{\partial \bar{X}}+\bar{V}\frac{\partial}{\partial \bar{Y}}\right)\bar{U}=-\frac{\partial \bar{P}}{\partial \bar{X}}+\frac{\partial \bar{\tau}_{\bar{X}\bar{X}}}{\partial \bar{X}}+\frac{\partial \bar{\tau}_{\bar{X}\bar{Y}}}{\partial \bar{Y}}-\frac{\sigma_{hnf}B_0}{(1+m^2)}\bar{U}+R_{\bar{X}} \tag{7}$$

$$\rho_{hnf}\left(\frac{\partial}{\partial \bar{t}}+\bar{U}\frac{\partial}{\partial \bar{X}}+\bar{V}\frac{\partial}{\partial \bar{Y}}\right)\bar{V}=-\frac{\partial \bar{P}}{\partial \bar{Y}}+\frac{\partial \bar{\tau}_{\bar{Y}\bar{X}}}{\partial \bar{X}}+\frac{\partial \bar{\tau}_{\bar{Y}\bar{Y}}}{\partial \bar{Y}}-\frac{\sigma_{hnf}B_0}{(1+m^2)}\bar{V}+R_{\bar{Y}} \tag{8}$$

$$(\rho c_P)_{hnf}\left(\frac{\partial}{\partial \bar{t}}+\bar{U}\frac{\partial}{\partial \bar{X}}+\bar{V}\frac{\partial}{\partial \bar{Y}}\right)\bar{T}=\ k_{hnf}\left(\frac{\partial^2 \bar{T}}{\partial \bar{Y}^2}+\frac{\partial^2 \bar{T}}{\partial \bar{X}^2}\right)+(\rho c)_f\left(D_B\left(\frac{\partial \bar{C}}{\partial \bar{X}}\frac{\partial \bar{T}}{\partial \bar{X}}+\frac{\partial \bar{C}}{\partial \bar{Y}}\frac{\partial \bar{T}}{\partial \bar{Y}}\right)+\frac{D_T}{T_1}\left[\left(\frac{\partial \bar{T}}{\partial \bar{X}}\right)^2+\left(\frac{\partial \bar{T}}{\partial \bar{Y}}\right)^2\right]\right)+\frac{\sigma_{hnf}B_0^2}{(1+m^2)}\bar{U}^2+Q_0+\bar{\tau}_{\bar{X}\bar{X}}\frac{\partial \bar{U}}{\partial \bar{X}}+\bar{\tau}_{\bar{Y}\bar{Y}}\frac{\partial \bar{V}}{\partial \bar{Y}}+\bar{\tau}_{\bar{X}\bar{Y}}\left(\frac{\partial \bar{U}}{\partial \bar{Y}}+\frac{\partial \bar{V}}{\partial \bar{X}}\right) \tag{9}$$

$$\left(\frac{\partial}{\partial \bar{t}}+\bar{U}\frac{\partial}{\partial \bar{X}}+\bar{V}\frac{\partial}{\partial \bar{Y}}\right)\bar{C}=D_B\left(\frac{\partial^2 \bar{C}}{\partial \bar{Y}^2}+\frac{\partial^2 \bar{C}}{\partial \bar{X}^2}\right)+\frac{D_T}{T_1}\left(\frac{\partial^2 \bar{T}}{\partial \bar{Y}^2}+\frac{\partial^2 \bar{T}}{\partial \bar{X}^2}\right)-A\left(\frac{\bar{T}}{T_1}\right)^n Exp\left[\frac{-E_a}{k_B\bar{T}}\right](\bar{C}-C_0). \tag{10}$$

The stress components for the Williamson fluid are provided by.

$$\bar{\tau}_{\bar{X}\bar{X}}=2\mu_{hnf}(1+\Gamma\gamma)\frac{\partial \bar{U}}{\partial \bar{X}} \tag{11}$$

$$\bar{\tau}_{\bar{X}\bar{Y}}=\bar{\tau}_{\bar{Y}\bar{X}}=\mu_{hnf}(1+\Gamma\gamma)\left(\frac{\partial \bar{U}}{\partial \bar{Y}}+\frac{\partial \bar{V}}{\partial \bar{X}}\right) \tag{12}$$

$$\bar{\tau}_{\bar{Y}\bar{Y}}=2\mu_{hnf}(1+\Gamma\gamma)\frac{\partial \bar{V}}{\partial \bar{Y}} \tag{13}$$

Where $\gamma=\sqrt{\left(\frac{\partial \bar{U}}{\partial \bar{Y}}+\frac{\partial \bar{V}}{\partial \bar{X}}\right)^2+2\left(\left(\frac{\partial \bar{U}}{\partial \bar{X}}\right)^2+\left(\frac{\partial \bar{V}}{\partial \bar{Y}}\right)^2\right)}$

The altered Darcy's law, linking pressure drop to the velocity field, is a key element of the conventional model for porous media. It connects the decrease in pressure across the medium to the medium's permeability and the viscosity of the fluid. Concerning this issue, the Darcy resistances in component form are expressed by

$$R_{\bar{X}}=-\frac{\mu_{hnf}}{k^*}(1+\Gamma\gamma)\bar{U} \tag{14}$$

$$R_{\bar{Y}}=-\frac{\mu_{hnf}}{k^*}(1+\Gamma\gamma)\bar{V} \tag{15}$$

Here, denotes the permeability of the porous medium k^*, and μ_{hnf} represents the dynamic viscosity of the hybrid nanofluid. It is observed that in the instance of Newtonian fluids, i.e., $\Gamma=0$, the modified Darcy's term will revert to its conventional Darcy's porous term.

The suitable boundary constraints in dimensional form are

$$\bar{U}=0,\ \bar{T}=T_0,\bar{C}=C_0,\text{ at }\bar{Y}=\overline{H_1} \tag{16}$$

$$\bar{U}=0,\ \bar{T}=T_1,\bar{C}=C_1,\text{ at }\bar{Y}=\overline{H_2} \tag{17}$$

The physiological characterizations of hybrid nanofluid as given in Eq. (18) and Numerical values of physiological characterizations of base fluid, and nanoparticles are mentioned in Table 1.

Table 1. Thermophysical properties of hybrid nanoparticles.

Properties	Al_2O_3	H_2O	$C_2H_6O_2$
$\rho\left(\frac{kg}{m^3}\right)$	6320	997	1116.6
$C_p\left(\frac{J}{kgK}\right)$	765	4179	2382
$K\left(\frac{W}{mK}\right)$	76.5	0.607	0.254
$\sigma\left(\frac{S}{m}\right)$	35×10^6	0.05	1.07×10^{-7}

$$
\begin{aligned}
&\{\\
&\frac{\mu_{hnf}}{\mu_f}=\frac{1}{(1-\phi_1)^{2.5}(1-\phi_2)^{2.5}}\\
&\frac{\rho_{hnf}}{\rho_f}=(1-\phi_2)\left[(1-\phi_1)+\phi_1\frac{\rho_{n1}}{\rho_f}\right]+\phi_2\frac{\rho_{n2}}{\rho_f},\\
&\frac{(\rho c_p)_{hnf}}{(\rho c_p)_f}=(1-\phi_2)\left[(1-\phi_1)+\phi_1\frac{(\rho c_p)_{n1}}{(\rho c_p)_f}\right]+\phi_2\frac{(\rho c_p)_{n2}}{(\rho c_p)_f},\\
&k_{hnf}=\frac{k_{n2}+2k_{nf}-2\phi_2(k_{nf}-k_{n2})}{k_{n2}+2k_{nf}+\phi_2(k_{nf}-k_{n2})}k_{nf}\ \text{where}\ k_{nf}=\frac{k_{n1}+2k_f-2\phi_1(k_f-k_{n1})}{k_{n1}+2k_f+\phi_1(k_f-k_{n1})}k_f\\
&\sigma_{hnf}=\frac{\sigma_{n2}+2\sigma_{nf}-2\phi_2(\sigma_{nf}-\sigma_{n2})}{\sigma_{n2}+2\sigma_{nf}+\phi_2(\sigma_{nf}-\sigma_{n2})}\sigma_{nf}\ \text{where}\ \sigma_{nf}=\frac{\sigma_{n1}+2\sigma_f-2\phi_1(\sigma_f-\sigma_{n1})}{\sigma_{n1}+2\sigma_f+\phi_1(\sigma_f-\sigma_{n1})}\sigma_f,\\
&\}
\end{aligned}
\tag{18}
$$

Flow is erratic in fixed frames $(\bar{X},\bar{Y})$, whereas motion is continuous in wave frames $(\bar{x},\bar{y})$. The relationship between the fixed and wave frames is described as

$$
\bar{v}=\bar{V},\bar{u}=\bar{U}-c,\bar{y}=\bar{Y},\bar{x}=\bar{X}-c\bar{t},\bar{p}(\bar{x},\bar{y})=\bar{P}(\bar{X},\bar{Y},\bar{t}),T(\bar{x},\bar{y})=\bar{T}(\bar{X},\bar{Y},\bar{t}),
$$
$$
C(\bar{x},\bar{y})=\bar{C}(\bar{X},\bar{Y},\bar{t}). \tag{19}
$$

The dimensionless parameters are given below:

$$
x=\frac{\bar{x}}{\lambda},y=\frac{\bar{y}}{p_1},u=\frac{\bar{u}}{c},v=\frac{\bar{v}}{c\delta},p=\frac{\bar{p}{p_1}^2}{\lambda\mu_f c},\varepsilon_1=\frac{q_1}{p_1},\varepsilon_2=\frac{q_2}{p_1},d=\frac{p_2}{p_1},\delta=\frac{p_1}{\lambda},Re=\frac{\rho c p_1}{\mu_f},
$$
$$
Mn=B_0p_1\sqrt{\frac{\sigma_f}{\mu_f}},\theta=\frac{T-T_0}{T_1-T_0},\Omega=\frac{C-C_0}{C_1-C_0},Pr=\frac{\mu_f(c_p)_f}{k_f},Ec=\frac{c^2}{(c_p)_f(T_1-T_0)},Nt=\frac{(\rho c)_f D_T(T_1-T_0)}{k_f T_1},
$$
$$
Nb=\frac{(\rho c)_f D_B(C_1-C_0)}{k_f},\tau_{ij}=\frac{\bar{\tau}_{ij}p_1}{\mu_f c},h_1=\frac{\overline{H_1}}{p_1},h_2=\frac{\overline{H_2}}{p_1},S=\frac{Q_0p_1^2}{(T_1-T_0)k_f},\mathrm{Ka}=\frac{A{p_1}^2}{\vartheta_f},
$$

$$
Sc=\frac{\vartheta_f}{D_B},Ea=\frac{E_a}{k_BT_1},\beta=\frac{T_1}{T_0},\ Br=EcPr,We=\frac{\Gamma c}{p_1},Da=\frac{k^*}{{p_1}^2}. \tag{20}
$$

considering the stream function ψ associated with the velocity components u and v by

$$
u=\frac{\partial\psi}{\partial y},v=-\delta\frac{\partial\psi}{\partial x} \tag{21}
$$

The use of dimensionless quantities, Eq. (20), and taking into account the low Reynolds number and long wavele ngth approximations, the dimensionless governing equations look like this

$$
\frac{\partial p}{\partial x}=\frac{\partial}{\partial y}\left[x_1\left(1+We\frac{\partial^2\psi}{\partial y^2}\right)\frac{\partial^2\psi}{\partial y^2}\right]-\frac{x_2}{1+m^2}Mn^2\left(\frac{\partial\psi}{\partial y}+1\right)-\frac{1}{Da}\left(\frac{\partial\psi}{\partial y}+1\right)\left(1+We\frac{\partial^2\psi}{\partial y^2}\right) \tag{22}
$$

$$
\frac{\partial p}{\partial y}=0 \tag{23}
$$

$$
\frac{\partial^2\theta}{\partial y^2}+\frac{N_b}{x_3}\left(\frac{\partial\theta}{\partial y}\frac{\partial\Omega}{\partial y}\right)+\frac{N_t}{x_3}\left(\frac{\partial\theta}{\partial y}\right)^2+\frac{1}{x_3}\frac{x_2}{1+m^2}Mn^2Br\left(\frac{\partial\psi}{\partial y}+1\right)^2+\frac{1}{x_3}S+Br\left[x_1\left(1+We\frac{\partial^2\psi}{\partial y^2}\right)\frac{\partial^2\psi}{\partial y^2}\right]\frac{\partial^2\psi}{\partial y^2}=0 \tag{24}
$$

$$
\frac{\partial^2\Omega}{\partial y^2}+\frac{N_t}{N_b}\frac{\partial^2\theta}{\partial y^2}-\mathrm{Ka}\,Sc(1+(\beta-1)\theta)^nExp\left[\frac{-Ea}{1+(\beta-1)\theta}\right]\Omega=0 \tag{25}
$$

Also, $x_1 = \frac{\mu_{hnf}}{\mu_f}$, $x_2 = \frac{\sigma_{hnf}}{\sigma_f}$, and $x_3 = \frac{k_{hnf}}{k_f}$.

The boundary conditions in non–dimensional form are

$$\psi = -\frac{F}{2}, \frac{\partial \psi}{\partial y} = -1, \theta = 0, \Omega = 0 \quad at \quad y = h_1 \tag{26}$$

$$\psi = \frac{F}{2}, \frac{\partial \psi}{\partial y} = -1, \theta = 1, \Omega = 1 \quad at \quad y = h_2 \tag{27}$$

with wall shapes $h_1 = 1 + \varepsilon_1 Cos(x)$, $h_2 = -d - \varepsilon_2 Cos(x + \phi)$

The non - dimensional volume flow rate F in the wave frame is determined as

$$F = \int_{h_2}^{h_1} \frac{\partial \psi}{\partial y} dy \tag{28}$$

and is associated with the dimensionless mean flow rate Φ in the moving frame, is given by

$F = \Phi - 1 - d$.

2.1. Solution methodology

HPM, a powerful technique for solving both linear and nonlinear differential and integral equations, was creatively introduced by He (1999). Unlike other perturbation techniques, the HPM employs the homotopy concept and introduces some topological elements into the perturbation techniques. The homotopy function is given by $\hat{h}(\hat{x}, \hat{q}): \Omega \times [0,1] \rightarrow \Re$, where $\hat{q} \in [0,1]$ is used as an embedding parameter in the analysis. One of the distinguishing features of the HPM is that it converges rapidly without a small parameter in the homotopy equation.

Key Highlights of HPM:

- It unifies the classical perturbation method with the homotopy concept of topology.
- It does not need a perturbation parameter to be small, which is a requirement of the classical perturbation methods.
- It converts a nonlinear differential equation into a series of simpler linear equations.
- It represents the solution in the form of a rapidly convergent power series in the embedding parameter $\hat{q}$.
- It gives analytical or semi-analytical approximate solutions with high accuracy.
- It has been successfully applied to a wide range of nonlinear fluid flow, heat transfer, and boundary layer problems.

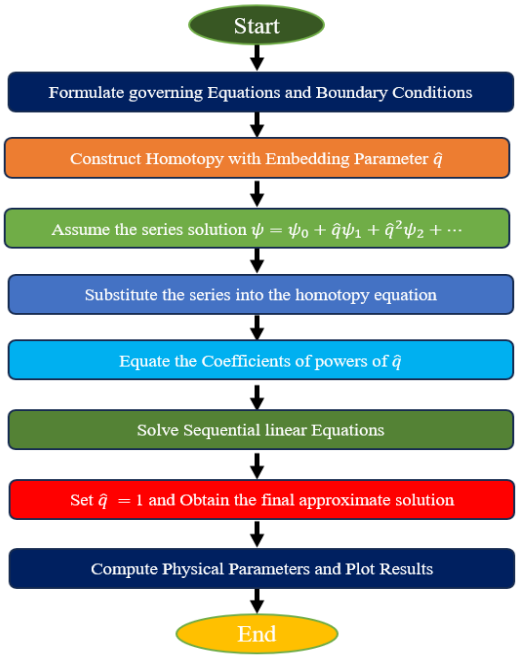

Figure 2. Flow chart for the solution procedure of HPM.

Now, Eqs. (22, 24) can be rewritten as

$$\frac{\partial^4\psi}{\partial y^4} + A_1\left[\frac{\partial^2\psi}{\partial y^2}\frac{\partial^4\psi}{\partial y^4} + \left(\frac{\partial^3\psi}{\partial y^3}\right)^2\right] - A_2\frac{\partial^2\psi}{\partial y^2} - A_3\left[\frac{\partial^3\psi}{\partial y^3} + \frac{\partial\psi}{\partial y}\frac{\partial^3\psi}{\partial y^3} + \left(\frac{\partial^2\psi}{\partial y^2}\right)^2\right] = 0 \tag{29}$$

$$\frac{\partial^2\theta}{\partial y^2} + A_4\frac{\partial\theta}{\partial y}\frac{\partial\Omega}{\partial y} + A_5\left(\frac{\partial\theta}{\partial y}\right)^2 + A_6\left(\frac{\partial\psi}{\partial y} + 1\right)^2 + A_7\left(\frac{\partial^2\psi}{\partial y^2}\right)^2 + A_8\left(\frac{\partial^2\psi}{\partial y^2}\right)^3 + A_9 = 0 \tag{30}$$

Using the assumption of small temperature variations, the nonlinear term in the activation energy is linearized using the Taylor series expansion. This linearizes the exponential term up to the first-order terms, and the equation is reduced to a tractable form to solve it using the HPM. That is, assuming the $(\beta - 1) \ll 1$ and apply the Taylor series expansion [11], Eq. (25) can be written as:

$$\frac{\partial^2\Omega}{\partial y^2} + \frac{N_t}{N_b}\frac{\partial^2\theta}{\partial y^2} - KaSc(1 + n(\beta - 1)\theta)Exp[-Ea](1 + Ea(\beta - 1)\theta)\Omega = 0 \tag{31}$$

Again, assuming the $(\beta - 1) \ll 1$ and apply the Taylor series expansion, Eq. (31) becomes

$$\frac{\partial^2\Omega}{\partial y^2} + F_{10}\frac{\partial^2\theta}{\partial y^2} - \mathrm{Ka}ScExp[-Ea](1 + (n + Ea)(\beta - 1)\theta)\Omega = 0 \tag{32}$$

Now, Eq. (32) can be written as follows:

$$\frac{\partial^2\Omega}{\partial y^2} + A_{10}\frac{\partial^2\theta}{\partial y^2} - A_{11}\,\Omega - A_{12}\,\Omega\theta = 0 \tag{33}$$

In Eqs. (29), (30) and (33)

$A_1 = 2We$, $A_2 = \left(\frac{x_2 Mn^2}{x_1(1+m^2)} + \frac{1}{Da\,x_1}\right)$, $A_3 = \frac{We}{Da\,x_1}$, $A_4 = \frac{N_b}{x_3}$, $A_5 = \frac{N_t}{x_3}$, $A_6 = \frac{x_2}{x_3(1+m^2)}Mn^2Br$,

$A_7 = Brx_1$, $A_8 = Brx_1We$, $A_9 = \frac{1}{x_3}S$, $A_{10} = \frac{N_t}{N_b}$, $A_{11} = KaScExp[-Ea]$,

$A_{12} = KaScExp[-Ea](n + Ea)(\beta - 1)$.

In HPM, the homotopy for the stream function (29), temperature (30), and concentration profiles (33) is as given below:

$$\hat{h}(\psi,\hat{q}) = (1-\hat{q})\left[\hat{L}_1(\psi) - \hat{L}_1(\psi_0)\right] + \hat{q}\left[\hat{L}_1(\psi) + A_1\left[\frac{\partial^2\psi}{\partial y^2}\frac{\partial^4\psi}{\partial y^4} + \left(\frac{\partial^3\psi}{\partial y^3}\right)^2\right] - A_2\frac{\partial^2\psi}{\partial y^2} - A_3\left[\frac{\partial^3\psi}{\partial y^3} + \frac{\partial\psi}{\partial y}\frac{\partial^3\psi}{\partial y^3} + \left(\frac{\partial^2\psi}{\partial y^2}\right)^2\right]\right] \tag{34}$$

$$\hat{h}(\theta,\hat{q}) = (1-\hat{q})\left[\hat{L}_2(\theta) - \hat{L}_2(\theta_0)\right] + \hat{q}\left[\hat{L}_2(\theta) + A_4\frac{\partial\theta}{\partial y}\frac{\partial\Omega}{\partial y} + A_5\left(\frac{\partial\theta}{\partial y}\right)^2 + A_6\left(\frac{\partial\psi}{\partial y} + 1\right)^2 + A_7\left(\frac{\partial^2\psi}{\partial y^2}\right)^2 + A_8\left(\frac{\partial^2\psi}{\partial y^2}\right)^3 + A_9\right] \tag{35}$$

$$\hat{h}(\Omega,\hat{q}) = (1-\hat{q})\left[\hat{L}_2(\Omega) - \hat{L}_2(\Omega_0)\right] + \hat{q}\left[\hat{L}_2(\Omega) + A_{10}\frac{\partial^2\theta}{\partial y^2} - A_{11}\,\Omega - A_{12}\,\Omega\theta\right] \tag{36}$$

For our convenience, we utilize the linear operators $\hat{L}_1 = \left(\frac{\partial^4}{\partial y^4}\right)$, $\hat{L}_2 = \left(\frac{\partial^2}{\partial y^2}\right)$. The initial estimates for the aforesaid equations that meet the boundary constraints can be articulated as follows:

$$\psi_0 = B_1 + B_2 y + B_3 y^2 + B_4 y^3$$

$$\theta_0 = B_5 + B_6 y,\ \Omega_0 = B_5 + B_6 y \tag{37}$$

where, $B_1 = \frac{Fh_1^3 - 3Fh_1^2h_2 + 2h_1^3h_2 + Fh_2^3 - 3Fh_2^2h_1 + 2h_2^3h_1}{2(h_1-h_2)^3}$, $B_2 = \frac{-2h_1^3 + 12Fh_1h_2 - 6h_1^2h_2 + 6h_2^2h_1 + 2h_2^3}{2(h_1-h_2)^3}$

$B_3 = \frac{-6Fh_1 + 6h_1^2 - 6Fh_2 - 6h_2^2}{2(h_1-h_2)^3}$, $B_4 = \frac{4F - 4h_1 + 4h_2}{2(h_1-h_2)^3}$, $B_5 = \frac{h_1}{h_1-h_2}$, $B_6 = -\frac{1}{h_1-h_2}$

For a complete solution, the following series is constructed:

$$\psi(\mathrm{x},\mathrm{y}) = \psi_0 + \hat{q}\psi_1 + \hat{q}^2\psi_2 + \cdots \tag{38}$$

$$\theta(\mathrm{x},\mathrm{y}) = \theta_0 + \hat{q}\theta_1 + \hat{q}^2\theta_2 + \cdots \tag{39}$$

$$\Omega(\mathrm{x},\mathrm{y}) = \Omega_0 + \hat{q}\Omega_1 + \hat{q}^2\Omega_2 + \cdots \tag{40}$$

By substituting Eqs. (38-40) into Eqs. (34-26) and then equating the coefficients of $\hat{q}$, a set of equations is established along with the appropriate boundary conditions. Following the techniques of the HPM, we obtain series solutions for the functions $\psi(\mathrm{y})$, $\theta(\mathrm{y})$, and $\Omega(\mathrm{y})$ as $\hat{q} \to 1$. The computational software Mathematica version 13.3 is utilized to solve this system of equations.

The formulae for Nusselt number (Nu) and Sherwood number (Sh) are obtained as follows:

$$\mathrm{Nu}_i = {h_i}' \frac{\partial\theta}{\partial y}\Big|_{y=h_i} \tag{41}$$

$\mathrm{Sh}_i = {h_i}' \frac{\partial\Omega}{\partial y}\Big|_{y=h_i}$ where $i = 1,2$.

3. Validation of results

Fig. 3 presents a comparison between the current standard results and the approximate solutions from the previously described study. For $Mn \to 0, \phi_1 = \phi_2 = 0, Da \to \infty$ and $m = 0$, the velocity profiles for the current model are displayed and evaluated against the results of Nadeem and Akram [21]. A good correlation between the current results and those of Nadeem and Akram [21] can be found in Fig. 3, which is enough to indicate that the current model and results are validated.

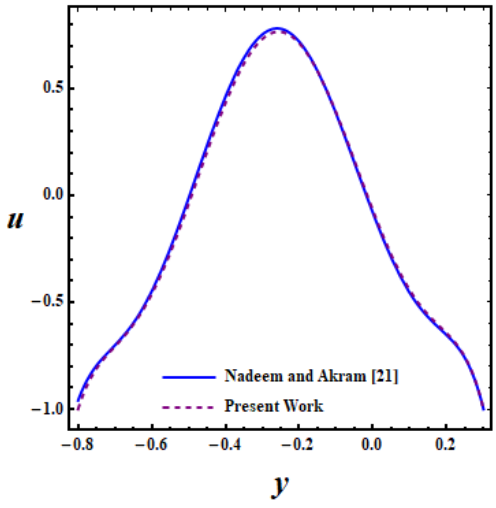

Figure 3. Validation of the velocity profile data from Nadeem and Akram [21] and the current model.

4. Results and discussions

The resulting linked nonlinear equations cannot be resolved analytically for an accurate solution. As a result, a semi–analytical method known as HPM is used to obtain approximate solutions. Visual representations of fluid flow properties are then generated for various parameters (refer to Table 2), such as velocity, temperature, concentration, trapping phenomenon, heat transfer coefficient (Nusselt number), and mass transfer coefficient (Sherwood number). These visualizations are obtained using DSolve commands built into Mathematica computer

software. Furthermore, this study aims to compare models in the presence of $C_2H_6O_2/Al_2O_3$, and $H_2O - C_2H_6O_2/Al_2O_3$ models in the presence of various nanoparticles. Also, if $\phi_1 = \phi_2 = 0$ corresponds to pure Al_2O_3, $\phi_1 = 0.01, \phi_2 = 0$ for $C_2H_6O_2/Al_2O_3$ (nanoparticle), and $\phi_1 = 0.01, \phi_2 = 0.02$ for $H_2O - C_2H_6O_2/Al_2O_3$ (hybrid nanoparticles).

Table 2. The description of physical parameters with range of values used for analysis [11, 21].

Parameter	Description	Range of values
$\boldsymbol{Re}$	It defines the proportion between inertial effects and viscous effects.	[0 - 1]
$\boldsymbol{Mn}$	It expresses the ratio of magnetic forces to viscous forces within the flow.	[0 - 5]
$\boldsymbol{Da}$	It indicates the fluid behavior through a porous medium.	[0 - 0.5]
$\boldsymbol{Pr}$	It describes the relative strength of momentum diffusion compared to thermal diffusion.	[0 – 10]
$\boldsymbol{Ec}$	It represents the proportion of kinetic energy to the enthalpy differences.	[0 – 2]
$\boldsymbol{Nb}$	It characterizes the influence of Brownian motion on nanoparticle motion.	[0 – 1]
$\boldsymbol{Nt}$	It evaluates the influence of temperature gradients on nanoparticle motion.	[0 – 1]
$\boldsymbol{Br}$	It denotes the relative importance of viscous dissipation compared to heat conduction in a fluid.	[0 -0.5]
$\boldsymbol{Sc}$	It represents the ratio of momentum diffusivity to the mass diffusivity in a fluid.	[0 – 2]
$\boldsymbol{Ea}$	It is the minimum energy required for molecules to initiate a chemical reaction or mass diffusion process.	[0 – 0.5]
$\boldsymbol{Ka}$	It measures the relative strength of a chemical reaction compared to the diffusion of a species in a fluid.	[0 – 5]
$\boldsymbol{S}$	It represents the effect of internal heat generation (source) or heat absorption (sink) within a fluid or medium.	[0 – 0.5]
$\boldsymbol{We}$	It measures the relative importance of elastic effects compared to viscous effects in a viscoelastic fluid flow.	[0 - 0.5]
$\boldsymbol{m}$	It represents the influence of the Hall effect on the motion of an electrically conducting fluid in a magnetic field.	[0 – 0.5]
$\boldsymbol{\beta}$	-	[0 - 0.5]
$\boldsymbol{\phi}$	-	[0 - π]
$\{\boldsymbol{\phi_1}, \boldsymbol{\phi_2}\}$	-	[0 – 0.1]

4.1. Velocity profile

In this segment, Figs. 4(a-f) delineate the effects of Mn, m, We, Da, ϕ, and $\{\phi_1, \phi_2\}$ on fluid flow velocity for nanofluid ($C_2H_6O_2/Al_2O_3$) and hybrid nanofluid ($H_2O - C_2H_6O_2/Al_2O_3$). Fig. 4a illustrates how the magnetic parameter Mn affects fluid velocity. The graphical arrangement shows that velocity significantly decreased with increasing magnetic parameter values, especially in the vicinity of the walls. This decreases results from a damping force known as the Lorentz force, which functions as a resistive force to lessen fluid motion. Fig. 4b illustrates that increasing the Hall parameter m boosts the axial velocity near the walls of the channel. This occurs because an increase in the Hall parameter reduces the effective magnetic damping, lowering electromagnetic resistance and increasing velocity. Weissenberg number We has two effects on velocity, as seen in Fig. 4c. The figure portrays the fluid velocity, which is decreasing near the channel's lower wall and enhancing it near the upper wall. Since the Weissenberg number We represents the ratio of elastic to viscous forces in a Williamson fluid. An increase in We enhances the fluid's elastic behaviour, modifying the momentum distribution in the channel. Consequently, the velocity decreases near the lower wall due to stronger elastic resistance, while velocity increases near the upper wall, indicating asymmetric momentum transport within the peristaltic channel. As the Darcy number Da increases, there is a noticeable increase in fluid velocity near both walls of the channel and conversely, an opposite trend is observed at the center of the channel (refer to Fig. 4d). The Darcy number represents the permeability of the porous medium. Higher Da corresponds to greater permeability and weaker drag resistance from the porous matrix, leading to an increase in the fluid velocity profile, whereas lower Da decreases the velocity due to enhanced porous resistance. So, it is important to note that a higher Darcy number corresponds to higher permeability and leads to higher velocity. Fig. 4e demonstrates the effect of the phase difference angle ϕ on the velocity profile. It is observed that as ϕ increases, the velocity at the lower wall begins to increase, and beyond the centerline, it alters its behavior, exhibiting a decreasing trend at the upper wall of the channel. The impact of the volume fractions of nanoparticles $\{\phi_1, \phi_2\}$ on the velocity profile is shown in Fig. 4f. At the center of the channel, it is experiencing a decreasing nature. An increase in the nanoparticle volume fraction enhances the effective viscosity and density of the hybrid nanofluid, which intensifies the internal resistance to motion.

Consequently, the axial velocity profile decreases across the channel due to stronger viscous interactions within the suspension. Further, the reverse trend occurs near both walls of the channel. It is important to know that from the Figs. 4(a-f), the lowest fluid velocity is linked to $C_2H_6O_2/Al_2O_3$, while the highest corresponds to a hybrid nanofluid ($H_2O - C_2H_6O_2/Al_2O_3$).

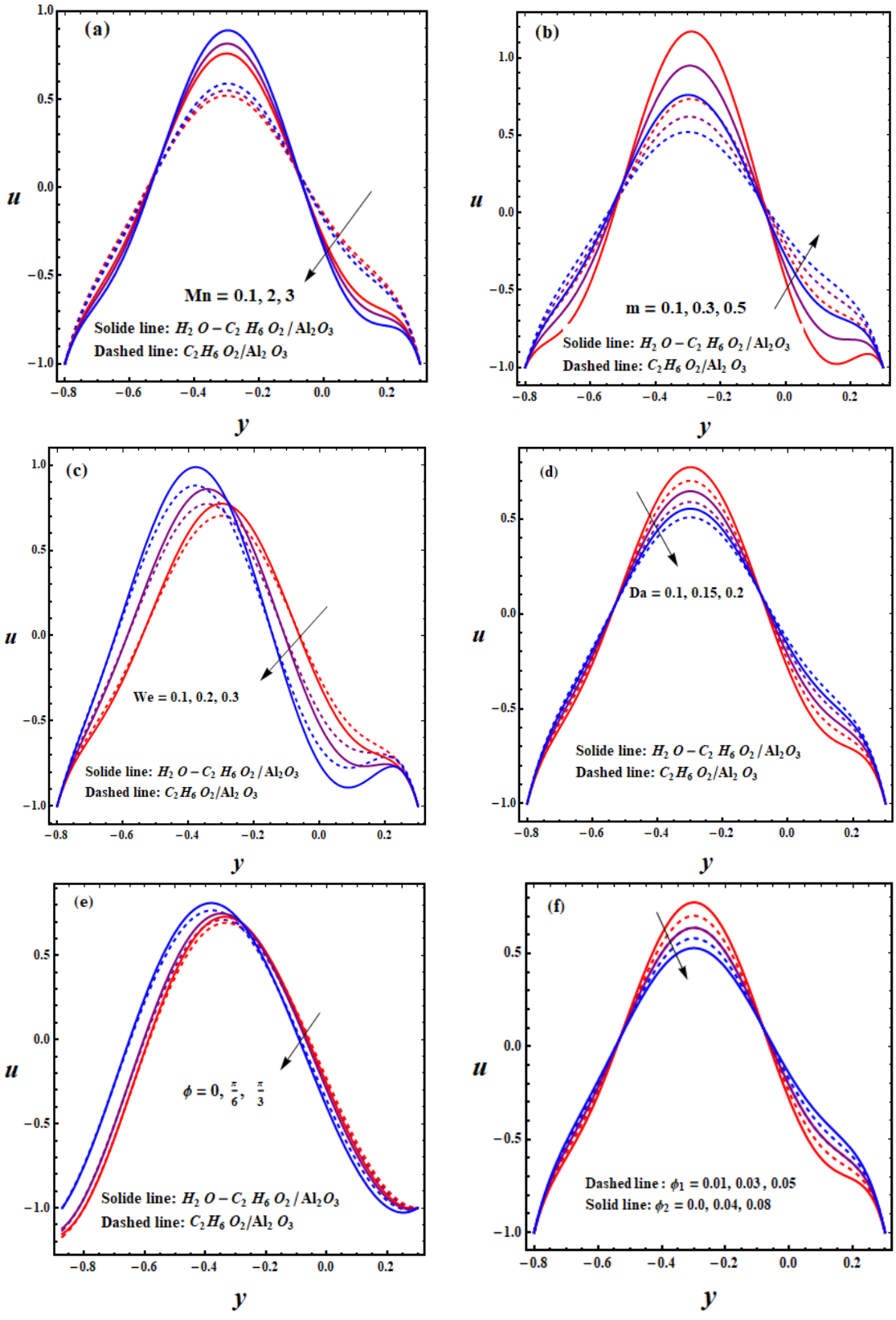

Figure 4. (a-f): Velocity profiles for diver's values of various parameters.

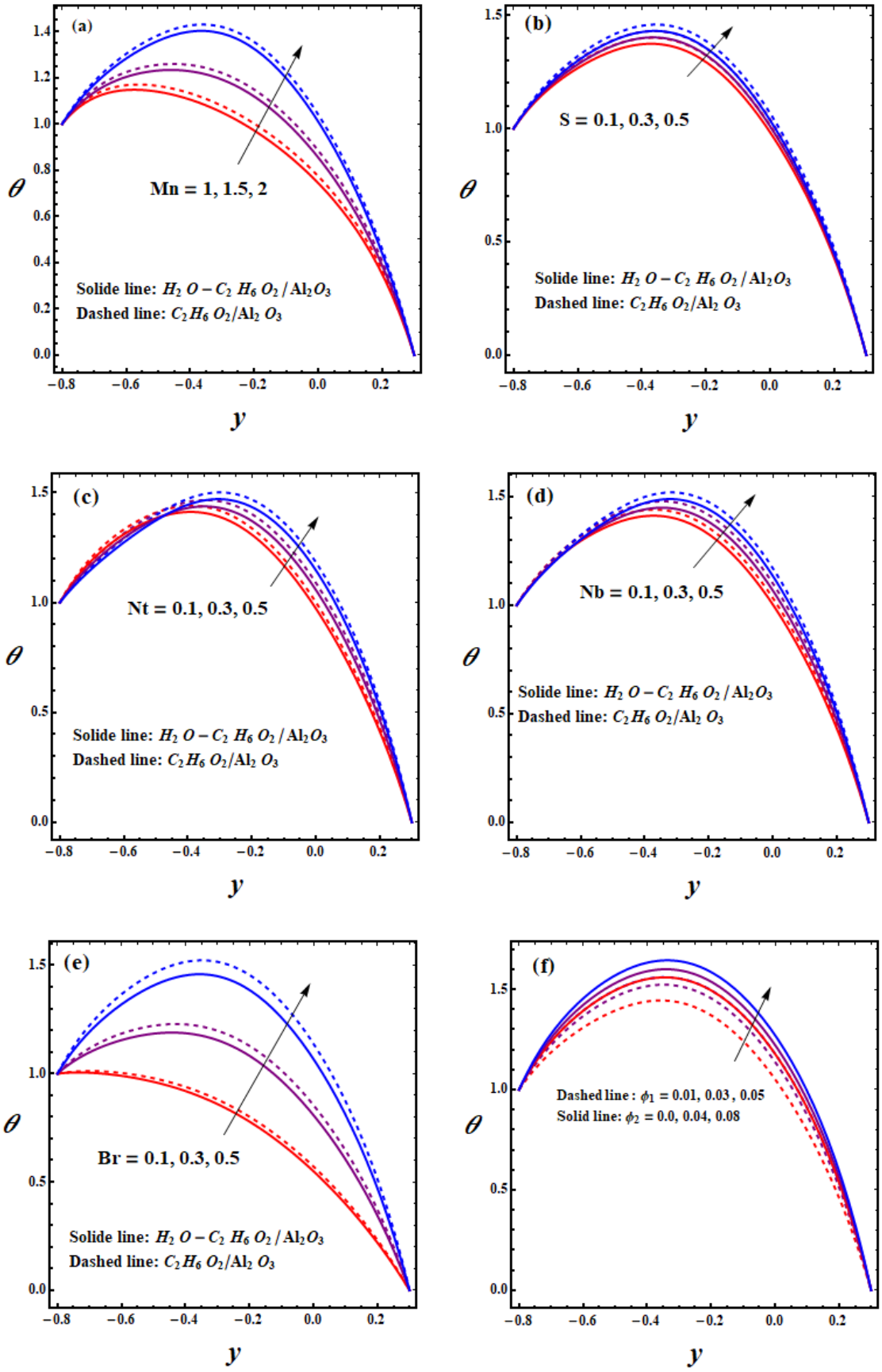

Figure 5. (a-f): Temperature configuration for various parameters.

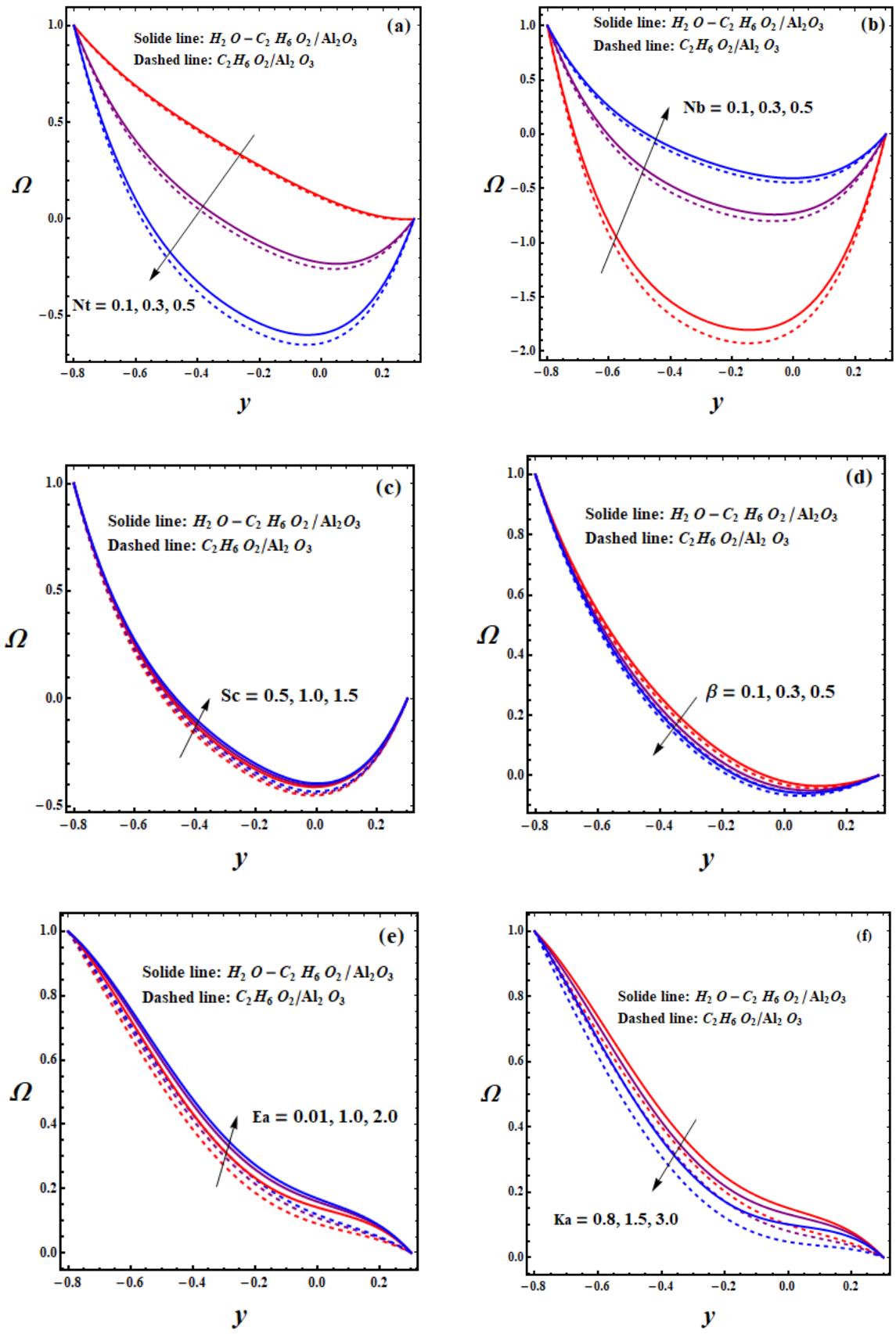

Figure 6. (a-f): Concentration profiles for different parameters.

4.2. Temperature profile

Figs. 5(a-f) demonstrates the influences of the magnetic parameter Mn, heat source/sink parameter S, thermophoretic parameter Nt, Brownian motion parameter Nb, Brinkmann number Br and nanoparticles volume fractions $\{\phi_1, \phi_2\}$ on the temperature profile within the channel for nanofluid ($C_2H_6O_2/Al_2O_3$) and hybrid nanofluid ($H_2O - C_2H_6O_2/Al_2O_3$). The increasing behavior of fluid temperature associated with the increasing Mn values, which is illustrated in Fig. 5a. This phenomenon is attributed to the prevailing characteristics of the Lorentz force governing fluid dynamics when Mn is intensified. The effect of heat source parameter S on fluid temperature is seen in Fig. 5b. It is clear that when the values of S increase, the fluid's temperature increases as well. An increase in the heat source parameter causes more thermal energy to be produced inside the fluid, which increases the energy of the particles in the fluid, causing the temperature of the fluid to increase. Figs. 5 (c-d) illustrate how the thermophoretic parameter Nt and Brownian motion parameter Nb affect temperature profiles. The fluid velocity increases away from the wall region, which is responsible for temperature increases, when thermophoretic and Brownian motion parameters increase the thermal conductivity of nanoparticles. Fig. 5e includes the temperature increase associated with higher Brinkmann number Br values. Since it includes the viscosity component, an increase in Br leads to viscosity having a greater influence on the flow field. This resistance results in an increase in the collision rate among the nanoparticles, which contributes to energy dissipation, ultimately causing an increase in temperature. Fig. 5f illustrates the impact of the volume fractions of nanoparticles $\{\phi_1, \phi_2\}$ on temperature. It is observed that the velocity decreases with increasing nanoparticle volume fractions; this indicates that as the values of $\{\phi_1, \phi_2\}$ increase, the resistance within the flow field also increases. Consequently, due to this increased resistance, the nanoparticles experience a greater loss of energy. This phenomenon leads to an increase in the temperature of the fluid. It is important to note that, according to the figures, the hybrid nanofluid $C_2H_6O_2/Al_2O_3$ has the lowest fluid temperature, whereas the highest is associated with $H_2O - C_2H_6O_2/Al_2O_3$. As a result, compared to ordinary nanofluid, the hybrid nanofluid exhibits superior thermal properties.

4.3. Concentration profile

Figs. 6(a-f) shows the impact of thermophoretic parameter Nt, Brownian motion parameter Nb, Schmidt number Sc, temperature ratio parameter β, activation energy parameter Ea, and chemical reaction parameter Ka on the concentration distribution in the channel for nanofluid $C_2H_6O_2/Al_2O_3$ and hybrid nanofluid $H_2O - C_2H_6O_2/Al_2O_3$). As seen in Figs. 6a and 6b, the concentration profile increases with the Brownian motion parameter Nb and decreases with the thermophoresis parameter Nt. Larger values of Nt cause the fluid's viscosity to disappear, which causes the volume fraction of the less dense particles to decrease. Fig. 6c illustrates that an increase in Sc results in a greater concentration distribution. This phenomenon arises because higher Sc values reduce mass diffusivity, which in turn enhances the concentration distribution. It is observed that the concentration profile decreases substantially as the temperature ratio parameter β is increased. Physically, it can be explained that as the value of β is increased, thermal effects in the fluid will be enhanced, and hence molecular diffusion will be increased, causing a decline in concentration in the boundary layer region, as shown in Fig. 6d. As the activation energy parameter Ea increases, the concentration also shows an increase due to reduction of effective chemical reaction rate which leads to less consumption of species (refer to Fig. 6e). A decrease in concentration is noted for higher values of the chemical reaction parameter Ka, which accelerates the consumption of solute particles in the fluid (see in Fig. 6f).

4.4. Streamlines

The movement and creation of trapped bolus and streamlines are the most crucial phenomena in fluid dynamics when it comes to fluid flow via peristaltic mechanisms. Boluses form because of some of the streamlines closing during the process. The speed of these boluses is equal to that of a peristaltic wave. Improved knowledge of bolus formation makes it easier to understand peristaltic events, which advances engineering and medicine. From Figs. 7(a-c), it is observed that as the values of Mn parameter increase, the size of the trapped boluses decreases due to the lack of kinetic energy for the formation of larger recirculation zones. At the same time, the fragmented nature of the flow creates a larger number of boluses. In instances where the Darcy parameter is increased, the number of streamlines correspondingly increases, yet the dimensions of the boluses experience a reduction (refer to Figs. 8(a-c)). A comparable phenomenon is evident as the Weissenberg number We increases, as illustrated in Figs. 9(a-c). The dimensions of the entrapped boluses increase as varying values of the phase

difference angle parameter ϕ, while the quantity of trapped boluses decreases, as depicted in Figs. 10(a-c). Further, the dimensions of the entrapped boluses increase while the quantity of these boluses declines as the value of the hall parameter varies (see Figs. 11 (a-c)).

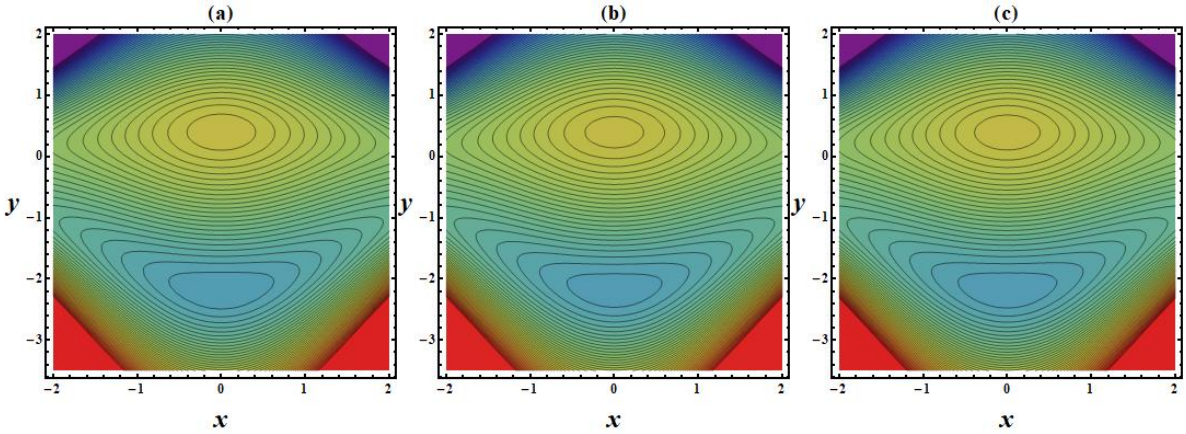

Figure 7. (a-c): Streamlines for diverse values of Mn.

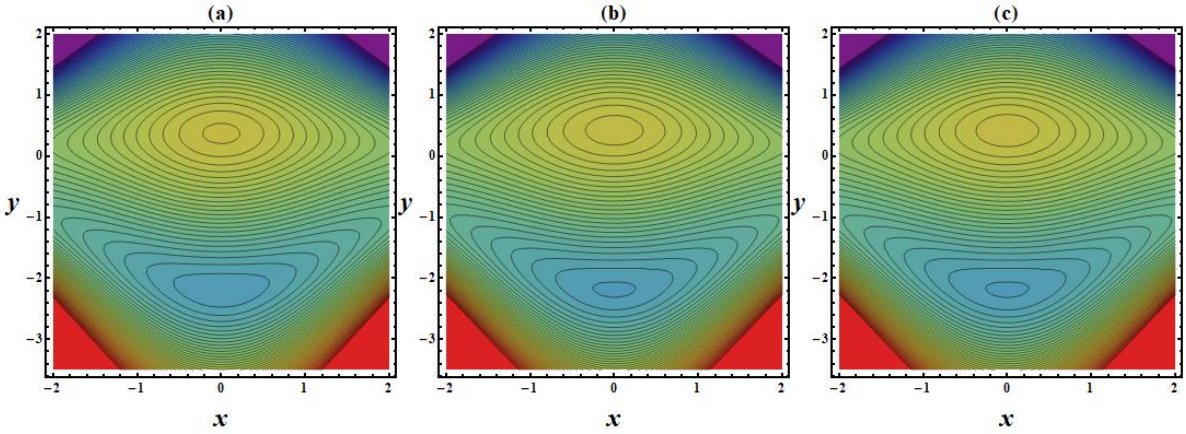

Figure 8. (a-c): Streamlines for diverse values of Da.

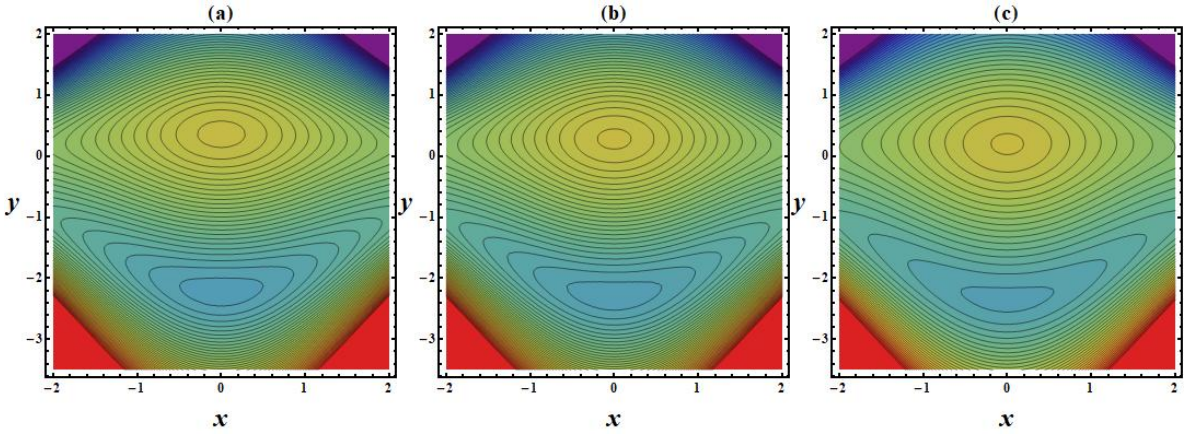

Figure 9. (a-c): Streamlines for diverse values of We.

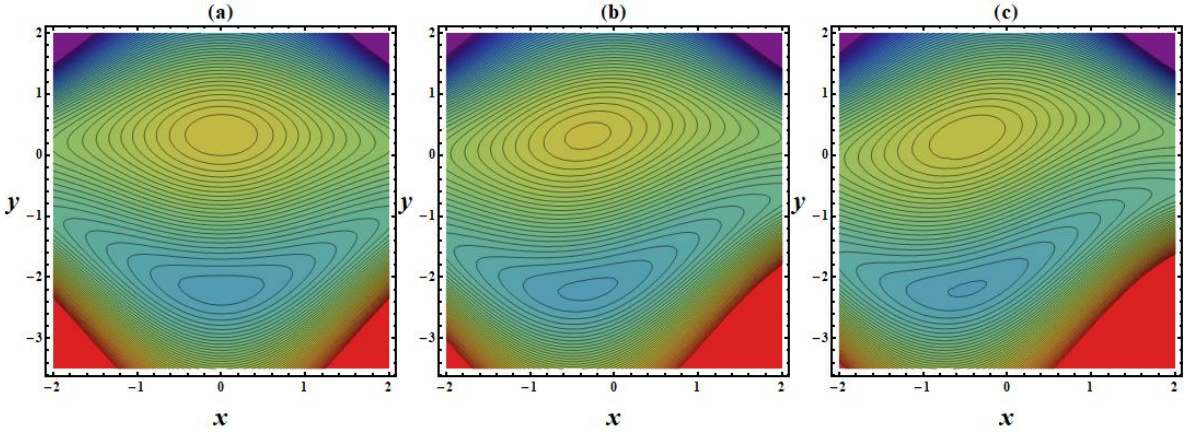

Figure 10. (a-c): Streamlines for diverse values of ϕ.

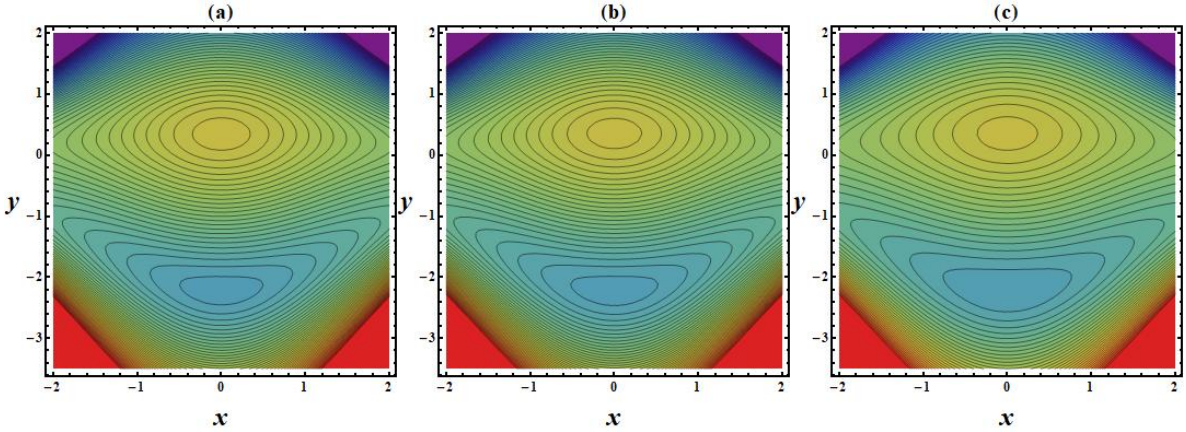

Figure 11. (a-c): Streamlines for diverse values of m.

Table 3. Nature of heat transfer coefficient (Nu) for different parameters.

Nt	Nb	S	ϕ_1	Mn	Br	$-Nu_1$ Upper wall	$-Nu_2$ Lower wall
0.4	**0.3**	**0.5**	**0.01**	**1**	**0.5**	**1.2001**	**1.1287**
0.1	0.3	0.5	0.01	1	0.5	1.0843	1.2805
0.3	0.3	0.5	0.01	1	0.5	1.1612	1.1797
0.5	0.3	0.5	0.01	1	0.5	1.2392	1.0773
0.4	**0.1**	0.5	0.01	1	0.5	1.1577	1.1730
0.4	**0.3**	0.5	0.01	1	0.5	1.2001	1.1287
0.4	**0.5**	0.5	0.01	1	0.5	1.2429	1.0835
0.4	0.3	**0.1**	0.01	1	0.5	1.0049	0.9069
0.4	0.3	**0.3**	0.01	1	0.5	1.2001	1.1287
0.4	0.3	**0.5**	0.01	1	0.5	1.3952	1.3505
0.4	0.3	0.5	**0.01**	1	0.5	1.2001	1.1287
0.4	0.3	0.5	**0.03**	1	0.5	1.2370	1.1573
0.4	0.3	0.5	**0.05**	1	0.5	1.2771	1.1884
0.4	0.3	0.5	0.01	**1**	0.5	1.2001	1.1287
0.4	0.3	0.5	0.01	**1.5**	0.5	1.8792	1.8272
0.4	0.3	0.5	0.01	**2**	0.5	2.8299	2.8050
0.4	0.3	0.5	0.01	1	**0.1**	0.5558	0.4234
0.4	0.3	0.5	0.01	1	**0.3**	0.8779	0.7761
0.4	0.3	0.5	0.01	1	**0.5**	1.2001	1.1287

4.5. Heat transfer coefficient and Mass transfer coefficient

Tables 3 and 4 illustrate the importance of different physiological traits on the mass transfer coefficient (Sh) and heat transfer coefficient (Nu), respectively. Examining Table 3 shows that the heat transfer coefficient Nu decreases with increasing thermophoresis parameter Nt and Brownian motion parameter Nb at the upper wall of the channel, while a contrary trend is seen at the lower wall of the channel. Moreover, the heat transfer coefficient reduces as the values of the heat source/sink parameter S, nanoparticle volume fraction ϕ_1, magnetic parameter Mn, and Brinkmann number Br escalate at both the upper and lower walls. Finally, Table 4 illustrates that higher values of the thermophoresis parameter Nt, temperature ratio parameter β, and activation energy parameter Ea enhance the mass transfer coefficient Sh at the upper wall, yet they exhibit an opposite trend at the lower wall. At the upper wall of the channel, rising values of the Brownian motion parameter Nb, Schmidt number Sc, and chemical reaction parameter Ka reduce the Sherwood number's magnitude, while enhancing it at the lower walls.

Table 4. Nature of mass transfer coefficient (Sh) for different parameters.

Nt	Nb	Sc	β	Ea	Ka	Sh_1	$-Sh_2$
						Upper wall	Lower wall
0.4	**0.3**	**0.5**	**0.1**	**0.5**	**0.8**	**0.9976**	**1.6582**
0.1	0.3	0.5	0.1	0.5	0.8	0.0434	0.0667
0.3	0.3	0.5	0.1	0.5	0.8	0.6770	1.1235
0.5	0.3	0.5	0.1	0.5	0.8	1.3206	2.1971
0.4	**0.1**	0.5	0.1	0.5	0.8	3.5101	5.8493
0.4	**0.3**	0.5	0.1	0.5	0.8	0.9976	1.6582
0.4	**0.5**	0.5	0.1	0.5	0.8	0.4937	0.8178
0.4	0.3	**0.5**	0.1	0.5	0.8	0.9976	1.6582
0.4	0.3	**1.0**	0.1	0.5	0.8	0.7850	1.3007
0.4	0.3	**1.5**	0.1	0.5	0.8	0.5609	0.9232
0.4	0.3	0.5	**0.1**	0.5	0.8	0.7950	1.3164
0.4	0.3	0.5	**0.3**	0.5	0.8	0.8988	1.4916
0.4	0.3	0.5	**0.5**	0.5	0.8	0.9976	1.6582
0.4	0.3	0.5	0.1	**0.01**	0.8	0.9364	1.5555
0.4	0.3	0.5	0.1	**1.0**	0.8	1.0477	1.7424
0.4	0.3	0.5	0.1	**2.0**	0.8	1.1203	1.8643
0.4	0.3	0.5	0.1	0.5	**0.8**	0.9976	1.6582
0.4	0.3	0.5	0.1	0.5	**1.5**	0.8122	1.3465
0.4	0.3	0.5	0.1	0.5	**3.0**	0.3851	0.6271

5. Conclusions

In the above article, the peristaltic transport of the MHD Williamson nanofluid model is studied when the fluid flows through a horizontally asymmetrical channel. Moreover, the fluid is flowing through a porous medium that is governed by the modified Darcy's law. In the present problem, hybrid nanoparticles are used to enhance the thermal properties of the fluid. In the Buongiorno nanofluid model, the thermophoresis and Brownian motion are included. Moreover, the energy and concentration equations are derived by taking into consideration the Joule heating, viscous heating, and activation energy. At the boundaries of the channel, the no-slip conditions are imposed. The following observations have been noted.

- The magnetic parameter decreases the velocity at both the upper and lower walls of the channel, while the Darcy parameter and Hall parameter produce an opposite effect. The Weissenberg number shows dual effects, as it decreases the velocity profile near the channel's lower wall and increases it near the upper wall.
- An increase in the magnetic parameter Mn suppresses axial velocity due to the Lorentz resistive force. Peak velocity declines by 18–22%, indicating stronger momentum resistance. Conversely, a higher Darcy number Da enhances permeability, accelerating fluid motion with a 15–19% rise in velocity magnitude.
- The temperature distribution increases with increasing thermophoresis, Brownian motion, heat source/sink, magnetic, and Brinkmann number parameters. Furthermore, compared to ordinary nanofluid, the hybrid nanofluid is found to have superior thermal properties.

- The concentration profile's magnitude decreases with an increase in the thermophoresis, temperature ratio, and chemical reaction parameters. On the other hand, the augmentation of the Schmidt number, activation energy parameter, and Brownian motion, on the other hand, shows the opposite trend.
- Activation energy significantly influences mass diffusion. Higher activation energy reduces the chemical reaction rate, resulting in an approximate 17–21% enhancement in nanoparticle concentration across the channel. Moreover, the temperature field also increases moderately (about 8–12%) due to reduced species consumption.
- At the upper wall of the channel, both the thermophoresis parameter and the Brownian motion parameter exhibit an increase, which results in a reduction of the heat transfer coefficient; conversely, a different trend is noted at the lower wall of the channel. Additionally, at both the upper and lower walls, the heat transfer coefficient diminishes as the magnetic parameter Mn, the nanoparticle volume fraction, the heat source/sink parameter S, and the Brinkmann number Br increase.
- An increase in the values of the Brownian motion parameter, Schmidt number, and Ka leads to a decrease in the magnitude of the Sherwood number at the upper wall of the channel, while an improvement is observed at the lower walls of the channel. In contrast, increasing values of the thermophoresis parameter, temperature ratio parameter, and activation energy parameter enhance the magnitude of the mass transfer coefficients at the upper wall, whereas the opposite trend is observed at the lower wall.
- The increase in values of Mn results in a larger size of the trapped boluses being reduced, while the number of boluses is increased. When the Darcy parameter is enhanced, the number of streamlines also increases, but the size of the boluses decreases.
- Overall, the study confirms that the collective improvement of thermal performance in peristaltic transport systems is achieved through hybrid nanoparticle dispersion, porous permeability, and non-Newtonian elasticity. These results highlight the potential of Williamson hybrid nanofluids for biomedical pumping mechanisms, microfluidic transport devices, and thermal management systems operating under MHD conditions.

Nomenclature

$(\bar{X}, \bar{Y})$	Cartesian coordinates in a fixed frame	Sh	Sherwood number
$(\overline{H_1}, \overline{H_2})$	Walls of the channel	F	Flow rate $(m^3 s^{-1})$
(x, y)	Cartesian coordinates in a moving frame	Br	Brinkman number
(p_1, p_2)	Upper and lower channel width (m)	Ka	Chemical reaction parameter
(q_1, q_2)	Wave amplitudes (m)	Ec	Eckert number
$\vec{J}$	Current density vector	We	Weissenberg number
$\vec{B}$	Magnetic field vector		
B_0	Magnetic field strength $(Nm^{-1}A^{-1})$	**Greek symbols**	
$\vec{E}$	Electric field vector	ρ	Density $\left(\frac{kg}{m^3}\right)$
m	Hall parameter	σ	Electrical conductivity $\left(\frac{S}{m}\right)$
c	Wave speed (ms^{-1})	μ	Dynamic viscosity $(Pa \cdot s)$
$\vec{q}$	Velocity vector	δ	Wave number
$\bar{U}, \bar{V}$	Dimensional velocity components (ms^{-1})	$\bar{\tau}$	Cauchy stress tensor (Pa)
(u, v)	Non - dimensional velocity components (ms^{-1})	τ_{ij}	Stress components (Pa)
$\bar{P}$	Fluid pressure (Pa)	β	Temperature ratio parameter
k_B	Boltzmann constant	θ	Non–dimensional temperature
$\bar{T}$	Dimensional temperature (K)	Ω	Non–dimensional concentration
$\bar{C}$	Dimensional concentration	λ	Wave length (m)
(T_0, T_1)	Reference temperatures (K)	γ	Thermal extension coefficient $\left(\frac{1}{K}\right)$
(C_0, C_1)	Reference concentration	c_p	specific heat capacity of fluid $\left(\frac{J}{kgK}\right)$
Q_0	Constant heat source/sink	c_f	specific heat capacity of particles $\left(\frac{J}{kgK}\right)$
k	Thermal conductivity $\left(\frac{W}{mK}\right)$	ψ	Stream function $(m^2 s^{-1})$
D_T	Diffusion coefficient of thermophoretic	(ϕ_1, ϕ_2)	Nanoparticles volume fractions
D_B	Brownian motion diffusion coefficient	$\varepsilon_1, \varepsilon_2$	Amplitude ratios
k^*	The permeability of the porous material	ϕ	Phase difference
Mn	Magnetic number	**Subscripts**	
Da	Darcy number	hnf	Hybrid nano fluid
Nt	Thermophoretic parameter	nf	Nano–fluid
Nb	Brownian motion parameter	f	Base fluid
Sc	Schmidt number	n_1	Solid gold nanoparticles
Ea	Activation energy	n_2	Aluminium oxide nanoparticles
(h_1, h_2)	Non-dimensional walls of the channel		
S	heat source/sink parameter		
Nu	Nusselt number		

Acknowledgments

The author expresses his affectionate thanks to the DST-SERB, Govt. of India, New Delhi, for the financial support under Empowerment and Equity Opportunities for Excellence in Science for 2023-2026. F.No.EEQ/2022/620 Dated:07/02/2023.

Funding

The authors state that no funding is involved.

Conflict of interest

The authors have no competing interests to declare that are relevant to the content of this article.

Author contributions

All authors contributed equally and approved the final manuscript.

Declaration of using AI tools

The authors declare that they have not used any type of generative artificial intelligence for the writing of this manuscript, nor for the creation of images, graphics, tables, or their corresponding captions.

References

[1] S. U. Choi and J. A. Eastman, Enhancing thermal conductivity of fluids with nanoparticles. (No. ANL/MSD/CP-84938; CONF-951135-29). Argonne National Lab. Argonne, IL, United States: ANL, 1995.
[2] Buongiorno, J. (2006). Convective transport in nanofluids. DOI: 10.1115/1.2150834
[3] R. K. Tiwari and M. K. Das, "Heat transfer augmentation in a two-sided lid-driven differentially heated square cavity utilizing nanofluids," Int. J. Heat Mass Transf., vol. 50, no. 9-10, pp. 2002–2018, 2007. (gy) DOI: 10.1016/j.ijheatmasstransfer.2006.09.034
[4] M. G. Reddy and O. D. Makinde, "Magnetohydrodynamic peristaltic transport of Jeffrey nanofluid in an asymmetric channel," J. Mol. Liq., vol. 223, pp. 1242–1248, 2016. DOI: 10.1016/j.molliq.2016.09.080
[5] H. Vaidya, K. V. Prasad, D. Tripathi, R. Choudhari, Hanumantha, and H. Ahmad, "Viscoplastic Hybrid Nanofluids Flow Through Vertical Stenosed Artery," Bionanoscience, vol. 13, no. 4, pp. 1–23, 2023. DOI: 10.1007/s12668-023-01213-y
[6] K. V. Prasad, H. Vaidya, R. Choudhari, D. Tripathi, and S. Karanth, "Advancing Blood Flow in Stenotic Arteries through Magnetohydrodynamic Peristaltic Motion of Hybrid Nanoparticles," Chin. J. Phys., 2024.
[7] Divya, A., Ramasekhar, G., Nagaraja, K. V., & Narasimhamurthy, S. K. (2025). Linear regression analysis of Williamson hybrid nanofluid flow with thermal radiation: Numerical simulation. International Journal of Thermofluids, 101343.
[8] M. Alghamdi, B. Fatima, Z. Hussain, Z. Nisar, and H. A. Alghamdi, "Peristaltic pumping of hybrid nanofluids through an inclined asymmetric channel: A biomedical application," Mater. Today Commun., vol. 35, p. 105684, 2023. DOI: 10.1016/j.mtcomm.2023.105684
[9] A. Rehman, M. Inc, A. Mohammad, and R. Jan, "Heat transfer in couple stress Williamson hybrid nanofluid with slip viscous dissipation and radiation and slip impacts: Semi-numerical simulation," Mod. Phys. Lett. B, vol. 39, no. 31, p. 2550182, 2025. DOI: 10.1142/S0217984925501829
[10] T. Hayat, S. Nawaz, and A. Alsaedi, "Entropy generation and endoscopic effects on peristalsis with modified Darcy's law," Physica A, vol. 536, p. 120846, 2019. DOI: 10.1016/j.physa.2019.04.082
[11] N. Eldabe, M. Abouzeid, M. Abdelmoneim, and M. E. Ouaf, "Electro-osmotic peristaltic flow of non-Newtonian nanofluid Al2 O3 inside a microchannel with modified Darcy's law and activation energy," Egypt. J. Chem., vol. 67, no. 4, pp. 251–271, 2024.
[12] A. Tanveer, S. Mahmood, T. Hayat, and A. Alsaedi, "On electroosmosis in peristaltic activity of MHD non-Newtonian fluid," Alex. Eng. J., vol. 60, no. 3, pp. 3369–3377, 2021. DOI: 10.1016/j.aej.2020.12.051
[13] R. Choudhari, H. Vaidya, K. V. Prasad, R. K. Gulab, K. Guedri, A. Rehman, et al., "Electroosmosis augmented MHD third-grade fluid with slip and variable properties: An application for blood flow in arteries," Journal of Computational Biophysics and Chemistry, vol. 22, no. 03, pp. 243–258, 2023. DOI: 10.1142/S273741652340001X
[14] T. W. Latham, (1966). Fluid motions in a peristaltic pump (Doctoral dissertation, Massachusetts Institute of Technology).
[15] M. Y. Jaffrin and A. H. Shapiro, "Peristaltic pumping," Annu. Rev. Fluid Mech., vol. 3, no. 1, pp. 13–37, 1971. DOI: 10.1146/annurev.fl.03.010171.000305
[16] H. J. Rath, (2013). Peristaltische Stromungen, Springer-Verlag, 19, DOI: 10.1007/978-3-642-81452-5.
[17] L. M. Srivastava and V. P. Srivastava, "Peristaltic transport of blood: Casson model--II," J. Biomech., vol. 17, no. 11, pp. 821–829, 1984. DOI: 10.1016/0021-9290(84)90140-4
[18] A. M. Abd-Alla, E. N. Thabet, and F. S. Bayones, "Numerical solution for MHD peristaltic transport in an inclined nanofluid symmetric channel with porous medium," Sci. Rep., vol. 12, no. 1, p. 3348, Mar. 1 2022. DOI: 10.1038/s41598-022-07193-5
[19] Y. Peng, H. Nabae, Y. Funabora, and K. Suzumori, "Peristaltic transporting device inspired by large intestine structure," Sens. Actuators A Phys., vol. 365, p. 114840, 2024. DOI: 10.1016/j.sna.2023.114840
[20] R. V. Williamson, "The flow of pseudoplastic materials," Ind. Eng. Chem., vol. 21, no. 11, pp. 1108–1111, 1929. DOI: 10.1021/ie50239a035
[21] S. Nadeem and S. Akram, "Peristaltic flow of a Williamson fluid in an asymmetric channel," Commun. Nonlinear Sci. Numer. Simul., vol. 15, no. 7, pp. 1705–1716, 2010. DOI: 10.1016/j.cnsns.2009.07.026

[22] N. T. Eldabe, O. M. Abo-Seida, A. A. Abo Seliem, A. A. Elshekhipy, and N. Hegazy, "Magnetohydrodynamic peristaltic flow of Williamson nanofluid with heat and mass transfer through a non-Darcy porous medium," Microsyst. Technol., vol. 24, no. 9, pp. 3751–3776, 2018. DOI: 10.1007/s00542-018-3835-0

[23] M. Rashid, K. Ansar, and S. Nadeem, "Effects of induced magnetic field for peristaltic flow of Williamson fluid in a curved channel," Physica A, vol. 553, p. 123979, 2020. DOI: 10.1016/j.physa.2019.123979

[24] R. Rajesh and Y. Rajasekhara Gowd, "Heat and mass transfer analysis on MHD peristaltic Prandtl fluid model through a tapered channel with thermal radiation," J. Appl. Comput. Mech., vol. 5, no. 5, pp. 951–963, 2019.

[25] N. Imran, M. Javed, M. Sohail, K. C. Gokul, and P. Roy, "Exploration of thermal transport for Sisko fluid model under peristaltic phenomenon," J. Phys. Commun., vol. 4, no. 6, p. 065003, 2020. DOI: 10.1088/2399-6528/ab9557

[26] N. T. Eldabe, G. M. Moatimid, M. Abouzeid, A. A. Elshekhipy, and N. F. Abdallah, "Semi-analytical treatment of Hall current effect on peristaltic flow of Jeffery nanofluid," Int. J. Appl. Electromagn. Mech., vol. 67, no. 1, pp. 47–66, 2021. DOI: 10.3233/JAE-201626

[27] A. R. Bestman, "Natural convection boundary layer with suction and mass transfer in a porous medium," Int. J. Energy Res., vol. 14, no. 4, pp. 389–396, 1990. DOI: 10.1002/er.4440140403

[28] T. Hayat, Z. Nisar, A. Alsaedi, and B. Ahmad, "Analysis of activation energy and entropy generation in mixed convective peristaltic transport of Sutterby nanofluid," J. Therm. Anal. Calorim., vol. 143, no. 3, pp. 1867–1880, 2021. DOI: 10.1007/s10973-020-09969-1

[29] M. Rafiq, A. Shaheen, Y. Trabelsi, S. M. Eldin, M. I. Khan, and D. K. Suker, "Impact of activation energy and variable properties on peristaltic flow through porous wall channel," Sci. Rep., vol. 13, no. 1, p. 3219, Feb. 24 2023. DOI: 10.1038/s41598-023-30334-3

[30] Abdelmoneim, M. M., Eldabe, N. T., Abouzeid, M. Y., & Ouaf, M. E. (2024). Electro-osmotic effect on the peristaltic flow of Williamson nanofluid through a porous medium in the presence of activation energy and modified Darcy's law.

[31] H. Waqas, S. U. Khan, S. A. Shehzad, M. Imran, and I. Tlili, "Activation energy and bioconvection aspects in generalized second-grade nanofluid over a Riga plate: A theoretical model," Appl. Nanosci., vol. 10, no. 12, pp. 4445–4458, 2020. DOI: 10.1007/s13204-020-01332-y